Title
Can a fractured caprock self-heal?

Authors
Elkhoury, Jean E
Detwiler, Russell L
Ameli, Pasha

Publication Date
2015-05-01

DOI
10.1016/j.epsl.2015.02.010

Peer reviewed

Can a Fractured Caprock Selfheal?

Jean E. Elkhoury[1], Russell L. Detwiler[2], Pasha Ameli

Department of Civil & Environmental Eng., University of California, Irvine, CA, USA.

Abstract

The ability of geologic seals to prevent leakage of fluids injected into the deep subsurface is critical for mitigating risks associated with greenhouse-gas sequestration and natural-gas production. Fractures caused by tectonic or injection-induced stresses create potential leakage pathways that may be further enhanced by mineral dissolution. We present results from reactive-flow experiments in fractured caprock (dolomitic anhydrite), where additional dissolution occurs in the rock matrix adjacent to the fracture surfaces. Preferential dissolution of anhydrite left a compacted layer of dolomite in the fractures. At lower flow rate, rock-fluid reactions proceeded to near equilibrium within the fracture with preferential flow paths persisting over the 6-month duration of the experiment and a negligible change in permeability. At higher flow rate, permeability decreased by a dramatic two orders of magnitude. This laboratory-scale observation of self-healing argues against the likelihood of runaway permeability growth in fractured porous caprock composed of minerals with different solubilities and reaction kinetics. However, scaling arguments suggest that at larger length scales this self-healing process may be offset by the formation of dissolution channels. Our results have relevance beyond the greenhouse-gas sequestration problem. Chemical disequilibrium at waste injection sites and in hydrothermal reservoirs will lead to reactive flows that may also significantly alter formation permeability.

`http://detwiler.eng.uci.edu/publications.html`
`http://dx.doi.org/10.1016/j.epsl.2015.02.010`

Keywords: Reactive flow, Caprock integrity, Mineral dissolution, Mechanical deformation, Permeability alteration, Dolomitic anhydrite.

1. Introduction

Injection of fluids into deep saline aquifers or depleted oil and gas reservoirs is a promising strategy for CO_2 sequestration [Hitchon et al., 1999; Bachu, 2000; Metz et al., 2005; Kumar et al., 2005] and waste fluids disposal [Tsang et al., 2008]. However, fluid injection increases pore pressure in the targeted geologic formation, creating vertical pressure gradients that can drive flow towards the surface. Successful long-term isolation of injected fluids requires geologic seals, or caprocks, with large vertical extent or very low permeability and ideally both. Lab-scale measurements of caprock permeability provide a means for predicting leakage rates through intact caprock. But, preexisting fractures in the caprock layer or fractures induced by the injection process can provide flow paths that are orders-of-magnitude more conductive than the intact rock.

Fracture permeability is influenced by the roughness of the fracture surfaces [e.g., Brown, 1987], the degree of mismatch (or shear displacement) between the surfaces [e.g., Wang et al., 1988; Mallikamas and Rajaram, 2005], the stress applied to the fracture [e.g., Cook, 1992; Durham and Bonner, 1994], and the gouge created during fracturing events [e.g., Faoro et al., 2009; Elkhoury et al., 2011]. Predicting the

potential for fractures to provide leakage pathways is further complicated by the possibility for fracture permeability to change with time due to injection-induced perturbations in stress and fluid chemistry. Stress perturbations lead to mechanical deformation and fracture propagation that can increase or decrease formation permeability [Bandis et al., 1983; Liu, 2005; Elkhoury et al., 2006, 2011; Candela et al., 2011; Renard et al., 2012; Mason et al., 2013]. Chemical disequilibrium between fluids and resident minerals leads to dissolution or precipitation that further alter fracture porosity and permeability [Lowell et al., 1993; Durham et al., 2001; Berkowitz, 2002; Chaudhuri et al., 2008; Wigand et al., 2009; Smith et al., 2013; Mason et al., 2013; Noiriel et al., 2013; Elkhoury et al., 2013].

The relative magnitudes of the timescales associated with advection through a fracture (τ_a) and reactions at mineral surfaces (τ_r) determines the nature of fracture permeability evolution (Figure S1). When thermodynamics favor mineral dissolution and the residence time is long relative to reaction time scales (i.e., $\tau_a/\tau_r \gg 1$), dissolution-induced aperture growth occurs predominantly along preferential flow paths. The resulting reaction-front instabilities create the potential for runaway permeability increases [Durham et al., 2001; Detwiler et al., 2003; Elkhoury et al., 2013]. Conversely, at higher flow rates ($\tau_a/\tau_r \ll 1$) dissolution occurs more uniformly throughout the fracture [Elkhoury et al., 2013] and may even be fastest in the smallest aperture regions [Detwiler et al., 2003]. Furthermore, computational simulations of reactive alteration show that, because residence times within a fracture depend upon the fluid velocity and fracture length, at higher flow rates reaction instabilities can still occur, but at length scales larger than typical laboratory experiments [Szymczak and Ladd, 2011; Elkhoury et al., 2013].

Under reservoir conditions, both pore pressure and fluid chemistry perturbations are likely. Laboratory-scale experiments aimed at quantifying fracture permeability evolution due to coupled deformation and dissolution demonstrate a confounding range of behaviors: increased permeability [Elkhoury et al., 2013], decreased permeability [Ellis et al., 2013] and nonmonotonic changes in permeability [Polak et al., 2004]. Due to either experimental constraints or expediency these studies often involve conditions that differ from those encountered in the reservoir. For example it is difficult to accurately measure small differential pressures in experiments carried out at pore pressures of O(10^7 Pa), so differential pressures are often O(10^5 Pa) or larger, resulting in pressure gradients of 10s or even 100s of MPa/m (head gradients of 10^3 to 10^4). However, it is difficult to imagine the field conditions under which such large pressure gradients would be sustained. This results in experiments where $\tau_a/\tau_r \ll 1$ and dissolution occurs relatively uniformly throughout the fracture (regardless of aperture variability) and may be fastest in small aperture regions. The resulting increasing stresses at eroding contacts leads to pressure solution [Yasuhara et al., 2004] or brittle failure [Detwiler, 2008] and subsequent permeability loss.

The choice of fluid chemistry also influences the evolution of fracture dissolution. When studying the influence of CO_2 injection, a natural choice for injected fluid is a brine in equilibrium with host minerals equilibrated with CO_2 at reservoir pressure, which leads to influent fluids with pH $\lesssim 4$ [Elkhoury et al., 2013; Smith et al., 2013]. However, fluids leaking through a fractured caprock are likely to exhibit a wide range of compositions. Monitoring of reservoir fluids over 10 years of intermittent water and CO_2 injection at the Weyburn site show $5 <$ pH < 6 [Burrowes and Gilboy, 2001]. This is due to a combination of buffering due to dissolution of $CaCO_3$ in the reservoir, mixing of injected water with CO_2-equilibrated brine, and propagation of increased pressures far beyond CO_2 plumes. This suggests that fluids expected to leak through a caprock will likely exhibit a wide range of compositions with near-equilibirum with CO_2 at reservoir pressure a low-pH end member. Using such low-pH fluids in laboratory experiments increases reaction rates with carbonates and decreases τ_r, thus shortening the required duration of experiments. However, it also has implications on permeability evolution as it will increase the value of τ_a/τ_r, leading to the formation of dissolution channels and increased permeability observed in some experiments [Elkhoury et al., 2013].

Despite the simplifications inherent in laboratory-scale studies, such experiments provide invaluable insights into the competing processes that lead to permeability alteration. However, the relevant simplifications must be placed in the proper context; for example, there is mounting evidence that, though initial fracture aperture variability plays an important role in establishing the initial fracture permeability, it plays a second-order role in controlling the evolution of the fracture aperture relative to the transport and reaction timescales [Szymczak and Ladd, 2011; Elkhoury et al., 2013].

In this study, we performed reactive flow experiments in fractured cores from a dolomitic anhydrite ($CaMg(CaO_3)_2$, $CaSO_4$) caprock. We explored the relative importance of advective and reactive timescales during flow of a reactive fluid (water) in a mineral assemblage commonly found in caprocks overlying oil and gas reservoirs. We present results from two experiments in fractured cores with flow rates (and τ_a) differing by two orders of magnitude to determine the potential for caprock self-healing under this range of parameters. We chose the duration of both experiments so that an equal amount of mass dissolved from each sample, which required the low-flow-rate experiment to run for 6 months. Unlike previous experiments with very reactive fluids in carbonate cores, our experiments exhibited measurable dissolution within the porous matrix adjacent to the fracture suggesting that the diffusion timescale in the porous matrix is faster than the reaction time scale. In both experiments, dissolution weakened the porous matrix adjacent to the fracture, which led to a two-order-of-magnitude permeability decrease at high flow rate and negligible permeability change at low flow rate.

2. Experimental Description

To minimize mineralogical heterogeneity between samples, we took both samples from a single 15-cm-long, 9-cm-diameter core from the evaporite that forms the first layer of caprock overlying the Weyburn-Midale reservoir in Saskatchewan, Canada [Wilson and Monea, 2004]. We drilled 3.8-cm-diameter sub-cores centered on tensile fractures within the larger core to minimize the impact of damage caused during fracturing. Sample lengths were 6.3 cm (EV1) and 4.9 cm (EV2) and the initial rock masses were 213 g and 163 g for EV1 and EV2, respectively (See Table 1 for complete details of the two experiments).

Although fractures provide preferential flow paths, the permeability of well-mated fractures subjected to a confining stress typical of reservoir conditions have permeabilities that are similar to intact cores [e.g., Durham and Bonner, 1994]. For the case of the dolomitic anhydrite cap rock used in our experiments, the intact permeability is on the order of $10^{-19}\,m^2$ [Smith et al., 2013]. Thus, effective leakage pathways will require some shear displacement of the fracture surfaces to create the potential for sustained flow at pressure gradients consistent with those expected in the field. We increased the permeability in our well-mated tensile fractures by shear offsetting the fracture surfaces prior to mating by 0.051 and 0.038 cm for EV1 and EV2, respectively. We placed shims between the endcaps and rock sample (Figure S2) to maintain these displacements when applying confining stress to the samples. These fractures differ from shear fractures induced under significant normal stress due to the absence of gouge; however, they provide the ability to carefully characterize the surface and fracture geometry prior to flow-through experiments.

Under reservoir conditions, in regions not directly overlying the CO_2 plume, dissolution will be relatively slow due to high ionic concentrations of typical reservoir fluids. To accelerate the dissolution and facilitate lab-scale experiments at reasonable timescales (months), we used de-ionized water as the reactive fluid. Furthermore, speciation calculations using PHREEQC [Parkhurst and Appelo, 1999], show that flowing water instead of CO_2-equilibrated brine increases the solubility of anhydrite, and only significantly influences the solubility of dolomite relative to anhydrite at very high pCO_2 (low pH) (see Appendix A for details).

To begin the experiments, we jacketed the fractured cores and secured them in a flow-through reactor and applied a 7 MPa confining stress (Figures S2 and S3). A high-pressure ISCO syringe pump

controlled the confining pressure, while two additional ISCO syringe pumps, connected in parallel, continuously pushed de-aired de-ionized water at a temperature of 21^{o}C through the fractured sample at a constant flow rate ($Q_{EV1} = 0.01$ ml/min and $Q_{EV2} = 0.6$ ml/min) with pressure controlled at the outlet (Figures S2 and S3 and Elkhoury et al. [2013] for additional details of the experimental apparatus).

Prior to each flow-through experiment, we characterized the fracture surfaces and reconstructed the aperture fields (Figure 1) using a high-resolution optical profilometer [Ameli et al., 2013; Elkhoury et al., 2013]. During experiments, we periodically analyzed effluent, using an ion chromatograph (Metrohm 850 Professional IC), for Mg^{2+}, Ca^{2+} and SO_4^{2-} concentrations, c, which provided direct estimates of the evolving dissolution rates, $R(t) = Q \times c(t)$. After the flow-through experiments, we characterized each sample differently. For EV1 we performed low-resolution x-ray computed tomography (CT) scans and then impregnated the sample, under vacuum, with red-colored epoxy and sliced it in sections perpendicular to the fracture. We used optical photographs of the slices to measure aperture profiles after the flow-through experiment. For EV2, we separated the two halves of the fractured core, with some difficulty, dried the core, and brushed off dolomite from the two halves of the sample. Then, we rescanned the fracture surfaces with the optical profilometer [Ameli et al., 2013] and obtained the thickness of the evaporite layer that was altered by dissolution during the experiment.

Due to the large difference in flow rates between the two experiments, we ran EV1 for 180 days and EV2 for 7 days to ensure a similar amount of total dissolution from both cores ($\sim 2.5\%$ of the initial total mass). To compare results from the two experiments, we normalized time, t, by $T = \dfrac{M_o}{R(t \sim 0)}$ where M_o is the initial total mass of the sample. The cumulative mass dissolved at time t is then $M(t) = \int_0^t R(\zeta)\, d\zeta$ and T is the time at which the entire rock mass would dissolve at the initial dissolution rate.

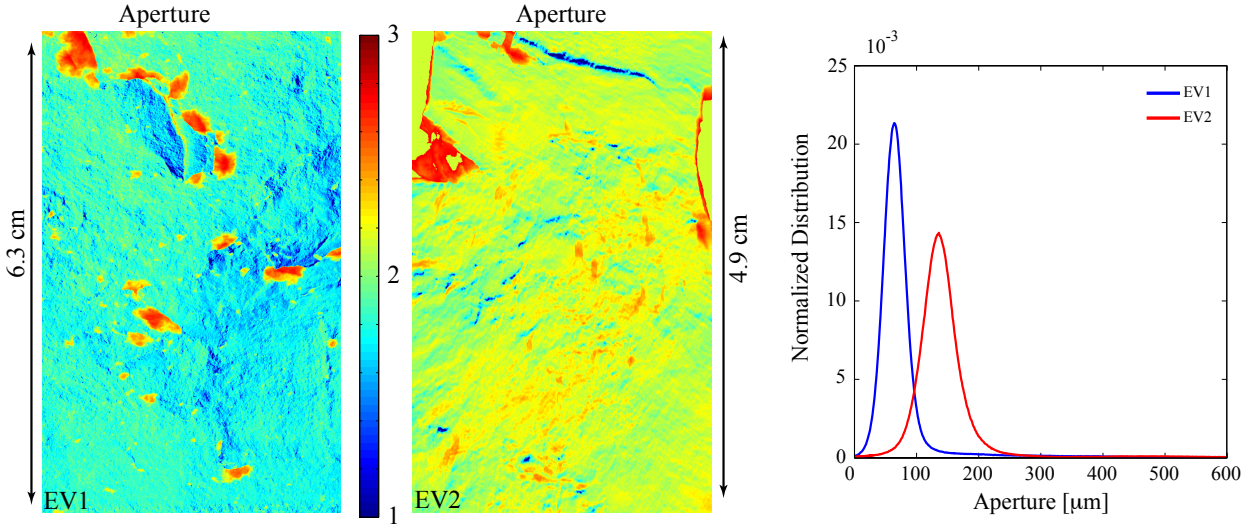

Figure 1: Initial aperture fields measured for samples EV1 and EV2 and the corresponding histograms. The colors represent values of log(aperture), with aperture measured in μm. These aperture fields correspond to the fracture in the absence of an applied normal stress.

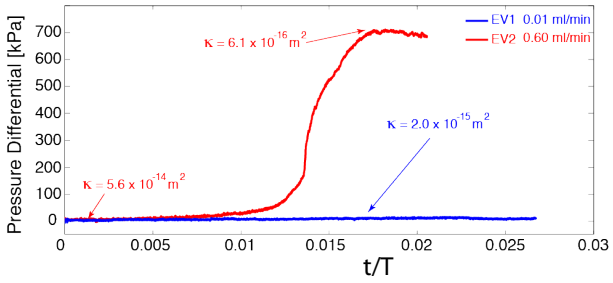

Figure 2: Pressure differential (ΔP) between inlet and outlet plotted against normalized time (t/τ) for samples EV1 and EV2 for flow rates of 0.01 ml/min and 0.6 ml/min respectively. The increase in ΔP for EV2 corresponds to a two order-of-magnitude decrease in permeability.

3. Results

Initial fracture aperture fields calculated for both samples allow a direct assessment of the relative similarity of the initial conditions for both experiments (Figure 1). Both fractures exhibit similar small-scale roughness and isolated regions of large fracture aperture caused by pieces of rock that were damaged during fracturing. The median fracture apertures in the absence of a confining stress are approximately 65 and 135 μm for EV1 and EV2, respectively. Because the small-scale aperture variability is similar for both fractures, we expect that the characteristics of the contact regions between the fracture surfaces are qualitatively similar for the two experiments when the 7 MPa confining stress was applied during flow-through experiments. The difference in fracture aperture between the two samples is consistent with the initial measured permeabilities of 2.0x10^{-15}m^2 and 5.6x10^{-14}m^2 for EV1 and EV2, respectively.

We observed a striking difference in the evolution of permeability between experiments EV1 and EV2 (Figure 2). For low flow rate (EV1), there was a negligible change in pressure differential over the 6-month duration of the experiment indicating near-constant permeability. In contrast, for high flow rate (EV2), the pressure differential across the fracture increased from ~ 5 kPa to ~ 700 kPa indicating more than two-order-of-magnitude decrease in permeability, κ, from 5.6×10^{-14} to 6.1×10^{-16} m^2 (Figure 2). It is especially noteworthy that the fracture with the larger initial aperture (EV2) exhibited the significant permeability reduction. To better understand this significant difference in permeability evolution, we analyzed the changes in the spatial distribution of mass within the two fractures.

At higher flow rate (EV2), dissolution of the anhydrite fracture surfaces left a porous layer of dolomite within the fracture aperture (Figure 3). Because the remaining layer of dolomite was more porous and weaker than the unaltered dolomitic anhydrite fracture surface, the confining stress caused compaction of the dolomite layer. This resulted in a decreased sample diameter (perpendicular to the fracture). The magnitude of the diameter decrease was largest at the inlet end of the core and similar in magnitude to the initial mean aperture (Figure 4). We hypothesize that the decrease in permeability was due to compaction of the residual uncemented dolomite within the fracture. To test this hypothesis, we optically measured the dolomite grain sizes (3 - 12 μm) and applied the Kozeny-Carman relation to estimate permeability of the compacted dolomite (7.5x10^{-17} - 1.2x10^{-15} m^2). The estimated range of κ encompasses the measured value of 6.1x10^{-16} m^2 (see Appendix B for details).

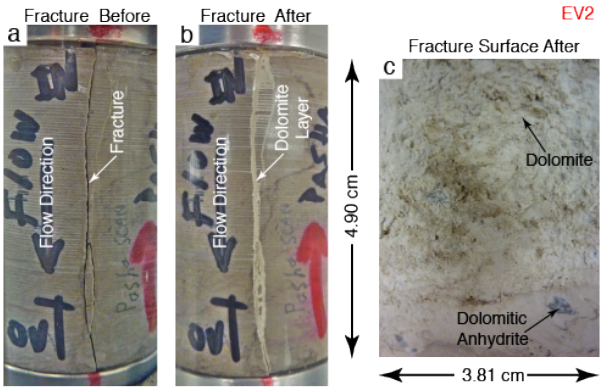

Figure 3: Photographs of the fracture in sample EV2 (a) before and (b) after the flow-through experiment, which highlight the formation of an off-white layer of dolomite filling the fracture. Separating the fracture surfaces revealed (c) an approximately 800-μm-thick layer of dolomite between the fracture surfaces.

At lower flow rate (EV1), dissolution of anhydrite also left a dolomite layer leading to a reduction in core

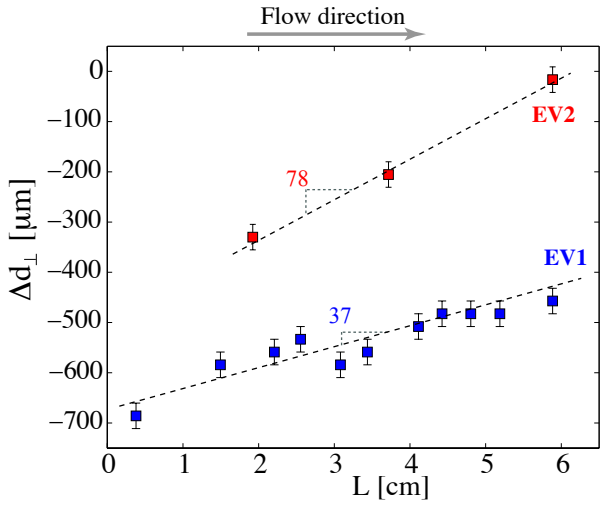

Figure 4: Change in sample diameter perpendicular to the fracture. Sample length is measured from the outflow. EV1 decreased in diameter on average three times more than EV2. The slope of $\Delta\, d_\perp$ is twice steeper for EV2 (78 μm/cm) compared to EV1 (37 μm/cm).

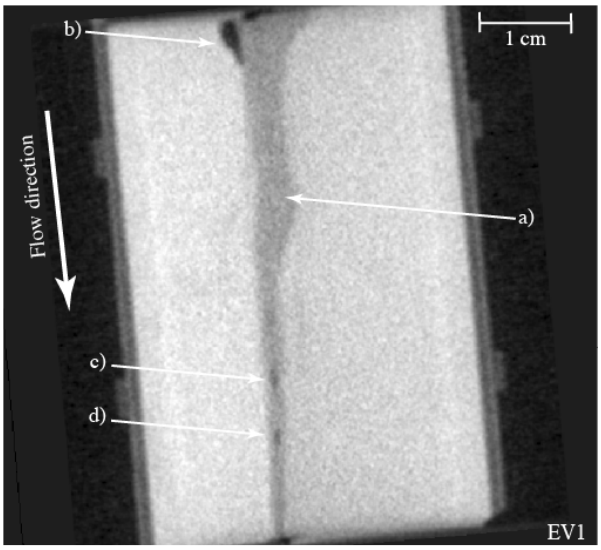

Figure 5: x-ray CT-scan cross-section of sample EV1 (low flow rate) after the flow-through experiment. Arrow a) points at the consolidated and compacted dolomite layer surrounding the fracture. It is the same region highlighted in Figure 7 by arrows 4 and 5. Arrow b) points at a dissolved region into the bulk close to the inlet. Arrows c) and b) point at aperture locations larger than 200 μm (resolution of the x-ray CT-scan).

diameter (perpendicular to the fracture) of approximately twice the initial mean aperture (Figure 4). Yet, unlike EV2, dissolution of anhydrite produced persistent conductive pathways through the dolomite layer (Figure 5 and 6). The initial fracture aperture exhibited small-scale aperture variability with isolated regions of aperture larger than $\sim 700\mu$m (Figure 6a). A low-resolution x-ray CT scan of the core (Figure 5) provided a coarse measure of the aperture distribution at the end of the 6-month experiment (Figure 6b). Though the resolution of this scan was too coarse (200 μm voxels) to resolve some regions of the aperture field. Figure 6c shows that we can use the x-ray CT scan to differentiate between regions of contact (blue), regions occupied by a mix of residual dolomite (green) and open aperture (red). The number and size of regions with aperture >200 μm increased by the end of the experiment and a broad channel in the center of the core contained a mix of residual dolomite and open aperture (Figures 7 and 8).

To further explore the details of the flow channels, Figure 7 shows before and after cross-sections of the fracture along the profile shown in Figure 6. Figure 7a shows a cross section of the profile from the initial reconstructed aperture field. If the dissolution were uniform throughout the fracture, a reduction in sample diameter would correspond to decreased aperture. Figure 7b shows the same aperture profile from figure 7a shortened by the change in core diameter. Optical photographs of sample sections perpendicular to the fracture, after impregnating the sample with epoxy, show a markedly larger aperture (Figures 7c, 7d). We point out four main observations in figure 7d: i) fracture healing (e.g. locations 1 and 2), ii) increase and persistence in aperture (e.g. location 3), iii) a dolomite layer bounded by diffusive fronts into the matrix (e.g. locations 4 and 5), and iv) presence of additional voids within the dolomite layer surrounding the fracture that are additional potential flow paths (e.g. location 6).

In addition to dissolution from the fracture walls, we highlight the propagation rate of the diffusive-

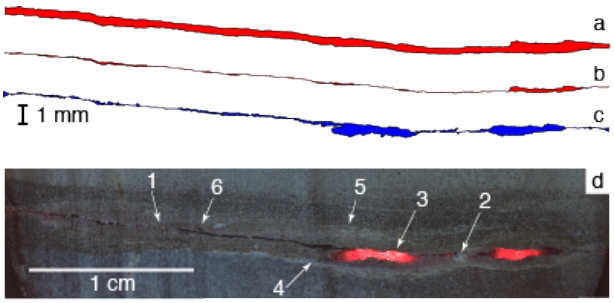

Figure 7: Fracture aperture and profiles of sample EV1 near the outlet (Figure 6): a) Aperture reconstructed from measured fracture surfaces before flow-through [Ameli et al., 2013]; b) Same as a) with a uniform aperture reduction of 550 μm (average sample diameter reduction perpendicular to the fracture); c) Measured aperture, after the flow-through experiment, obtained from slices of the fractured sample after impregnating with epoxy (d).

reactive front into the matrix. The diffusion length scale $W_d = \sqrt{D_M\, t_f}$, where t_f is the duration of the experiment and D_M the matrix diffusion coefficient, controls the thickness of the layer. D_M, is related to molecular diffusion, D_m, by $D_M = D_m \phi^n$ where ϕ is porosity and n the cementation factor. For Anhydrite $\phi^n \sim 10^{-3}$, hence $D_M = 10^{-12}\,\mathrm{m}^2/\mathrm{s}$. For EV1 ($t_f = 180\,\mathrm{days}$) $W_1 \sim 4000\,\mu\mathrm{m}$ is consistent with observed length scales in optical imaging of sample slices (Figure 7) and x-ray CT-scans (Figure 5). For EV2 ($t_f = 7\,\mathrm{days}$), $W_2 \sim 800\,\mu\mathrm{m}$ is consistent with optical imaging of the sample (Figure 3) and scanning of fracture surfaces before and after dolomite removal.

Figure 8a shows a photograph of a slice with conductive carbon tape on the side so the sample could be examined under an SEM with reduced charge accumulation without sputtering. Figure 8b is a high-resolution x-ray image perpendicular to flow (compared to figure 5) of the slice in figure 8a where we can clearly see the persistence of the fracture and the highlighted dolomite region surrounding the fracture (darker gray level). Unfortunately we gained access to the high-resolution x-ray system only after slicing the core (Figure 5) and we were only able to obtain the high resolution x-ray CT scan of one slice. An example of an EDS spectrum away from the fracture (blue square, figure 8c) shows a clear signal of

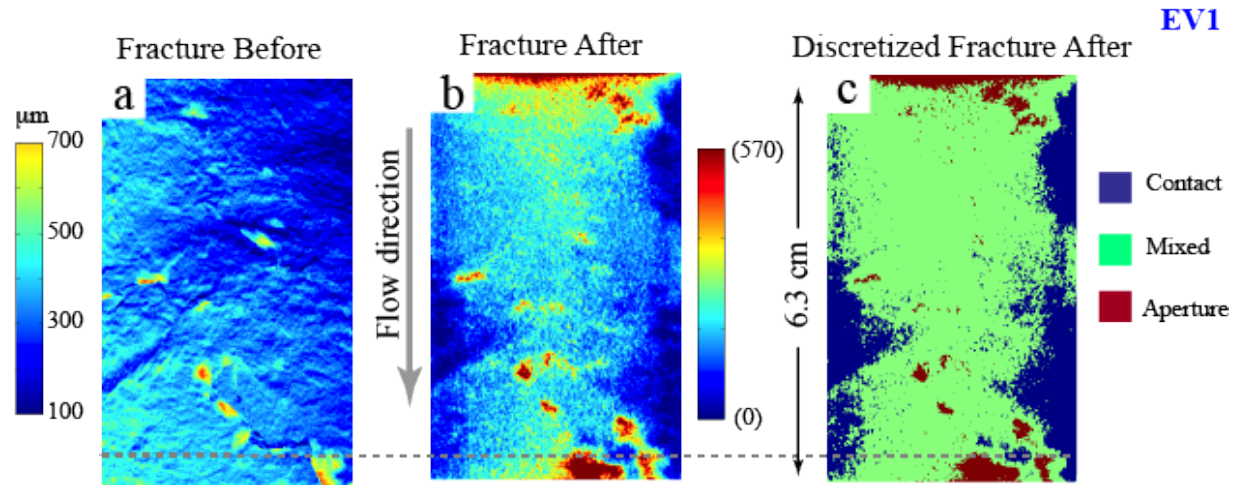

Figure 6: Fracture alteration of sample EV1 (low flow rate). a) initial aperture field obtained from mating the two fracture surfaces scanned with a white light profilometer; b) Fracture surface projected from a low-resolution 3D x-ray CT-scan of the sample after the flow-through experiment (the color scale was inferred from measured x-ray absorption coefficients); c) The discretization of panel b) into 3 regions, open aperture (red), mixed region (green) and contact (blue). The gray dashed line across the three panels identifies the location of the slice shown in figure 7.

the dolomitic anhydrite (presence of both Mg and S peaks) while spectra around the fracture (red circle, Figure 8d) show a clear absence of anhydrite (lack of the S peak). EDS spectra of the powder brushed off the fractured sample after pulling the two halves of the core apart (Figure S4) confirmed that the fracture infilling was predominantly dolomite.

Figure 9 plots the concentrations of Ca^{2+} and SO_4^{2-} against dimensionless time. Though we also measured Mg^{2+} concentrations, they were persistently more than two orders of magnitude smaller than Ca^{2+} concentrations and thus not shown in Figure 9. The effluent concentrations are normalized by the equilibrium concentration, which we measured by dissolving a finely ground piece of the core cut from the end of one of the samples in deionized water for approximately 2 weeks. The effluent from EV1 was near saturation during the entire 6-month experiments, with a slight decrease in concentrations at later time. We suspect this decreased concentration was due to the formation of the dissolution channel observed in Figures 6 and 7. EV2 exhibited effluent concentrations that were significantly below the equilibrium concentration over the duration of the experiment with an increase that coincided with the significant decrease in permeability.

The cumulative mass transfer (Figure 10), derived from measurements of effluent concentration with time, $c(t)$, reflects the strong difference in permeability evolution for the two experiments (Figure 2). As expected, at early times, for both experiments, the cumulative mass dissolved, $M(t)/M_o$, has a slope of 1 as a function of t/T, because the concentration of Ca^{2+} ions remains relatively constant during the initial phase of each experiment suggesting the dissolution rate is constant. At later times, the dissolution rate at low flow rate decreased by 20%. This is consistent with the development of dissolution chan-

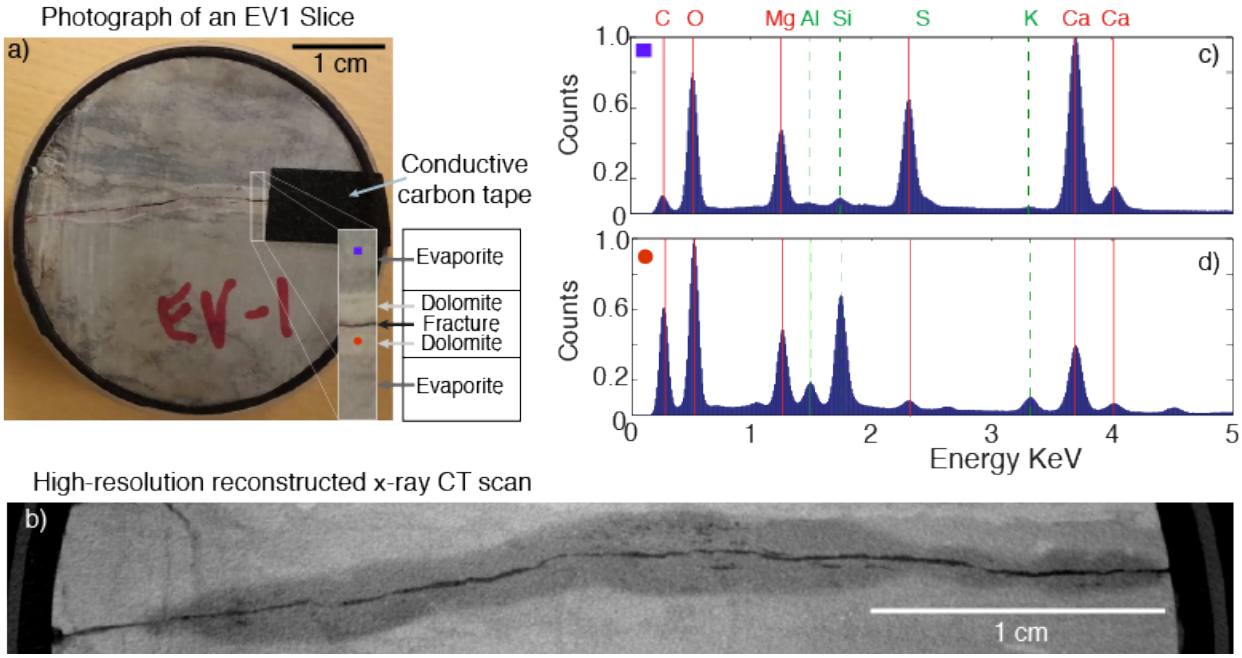

Figure 8: (a) Optical photograph and (b) high-resolution x-ray CT scan of an EV1 slice after flow-through. Inset in (a) is a zoomed region surrounding the fracture close to the conductive carbon tape. (c) and (d) are EDS spectra of the regions away from the fracture (blue square) where we can clearly see the signal of the dolomitic anhydrite and regions surrounding the fracture (red circle). Both dolomite and anhydrite are present in (c) and only dolomite in (d).

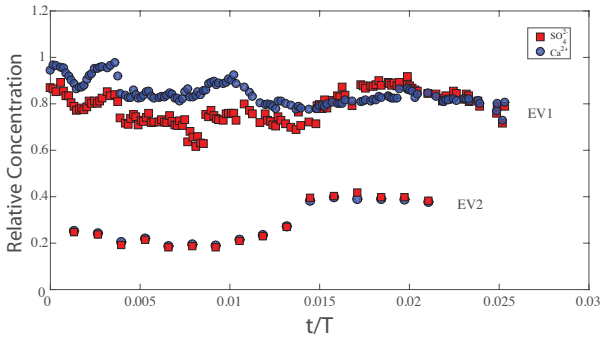

Figure 9: Temporal evolution of Ca^{2+} and SO_4^{2-} concentrations for both low flow rate (EV1) and high flow rate experiments (EV2). The overlap of both concentrations indicates negligible dolomite dissolution. This concentration, $c(t)$ is used to obtain the cumulative mass dissolved shown in figure 10

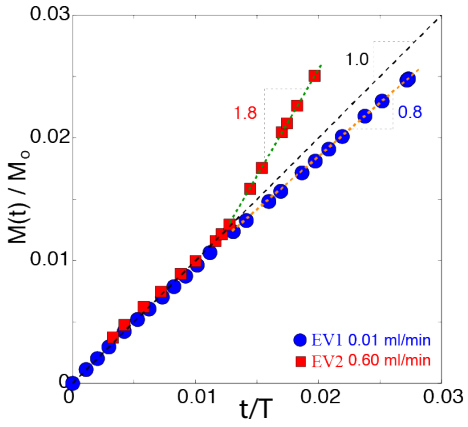

Figure 10: Normalized cumulative dissolved mass ($M(t)/M_o$) as a function of normalized time (t/τ). $M(t)$ is obtained from measurements of ion concentrations $c(t)$, using ion chromatography (Figure 9). The rate of dissolved mass at early stage does not change (black dashed line slope 1). However, the rate increased for high flow rate (EV2, slope 1.8, green dotted line) while it slightly decreased for the smaller flow rate case (EV1, slope 0.8, dotted orange line).

nels, which causes flow to bypass large regions of the fracture reducing effective reactive surface area. On the other hand, for high flow rate, dissolution was more uniform throughout the fracture and the larger ΔP caused more flow through the adjacent intact rock matrix (and more contact with dissolving anhydrite) resulting in an 80% increase in dissolution rate. Dissolution of anhydrite and the residual dolomite layer surrounding the fractures are prevalent in both experiments (Figure S5a). In the case of low flow rate (EV1) the fracture aperture persisted. Additionally, the dolomite layer surrounding the fracture included localized voids which may provide additional flow paths (Figure S5b). In the case of high flow rate (EV2), the dolomite layer was uniform leading to fracture closure (Figure S5c).

4. Discussion

Our experimental results showed a striking difference in behavior. We attribute this difference to the change in flow rate between the two experiments. Decreasing the flow rate increases the residence time of the fluid within the fracture, τ_a, without significantly changing the timescale of the dissolution reaction, τ_r. This dependence of dissolution on the Damköhler number ($Da = \tau_r/\tau_a$) has been observed in previous experimental studies where uniform dissolution is observed for large Da and channeled dissolution for small Da [Durham et al., 2001; Elkhoury et al., 2013]. Furthermore, at large Da the uniform dissolution can preferentially erode contacting asperities leading to the potential for decreased permeability [Detwiler, 2008]. However, these previous experimental studies showed permeability decreases that were relatively small compared to those observed in EV2. The substantial permeability decrease observed in EV2 resulted from relatively uniform dissolution throughout the fracture with concurrent dissolution of anhydrite within the porous matrix immediately adjacent to the fracture. For the dissolution reaction to propagate into the fracture matrix, the timescale associated with the dissolution reaction in the pores, τ_r, must be longer than the timescale of diffusive transport through a pore. This allows dissolved Ca^{2+} and SO_4^{2-} ions to diffuse from the pore space faster than these ions are produced by the dissolution reaction. Thus, a region of undersaturated fluid propagates into the porous matrix over time.

The dissolution process is further complicated in a polymineralic rock such as the dolomitic anhydrite

used in our experiments. Solubility differences for the different minerals can result in alteration of the structure of the porous matrix. In this case, dissolution of the more soluble anhydrite left residual uncemented dolomite grains filling the void space of the fracture. This has implication for the strength of the fracture because contact regions consisting of intact dolomitic anhydrite are transformed to uncemented dolomite grains. In our constant-confining-stress experiments, this resulted in normal deformation of the fracture, but it is also likely that the dissolution process significantly reduced the shear strength of the fracture. This weakening and compaction process differs fundamentally from compaction caused by pressure solution observed in saturated granular anhydrite subjected to high stresses [Pluymakers et al., 2014]. Such chemically-induced compaction occurs when the pore fluid is near equilibrium with anhydrite; diffusion of ions from contact regions leads to halos of supersaturation and mineral precipitation which gradually fills (heals) the pore space. However, advection of undersaturated fluid from an underlying carbonate reservoir will compete with this process, because it will enhance dissolution (of both gouge and fracture surfaces) and inhibit precipitation.

Any study consisting of a limited number of experiments must consider the potential impact of sample variability on the results. In our case, both samples were subcores from the same 15-cm length of core such that variability in sample mineralogy is representative of the small-scale heterogeneity within this formation. Furthermore, both fractures were tensile fractures subjected to a carefully controlled shear displacement such that small-scale aperture variability was similar despite a difference in mean apertures. A previous study in two fractures with very different initial apertures (a saw cut, bead-blasted core and a naturally fractured core) demonstrated that changing flow rate (or Da) had a much stronger influence on results than significant variations in initial aperture distributions [Elkhoury et al., 2013]. These experimental observations support analytical and computational analysis of the role of aperture variability on the development of reaction-front instabilities [Szymczak and Ladd, 2012]. Though the mineralogy of the cores used in our previous study differs from those used here, we expect that the importance of Da on the dissolution process relative to variations between samples transcends fluid and mineralogic compositions used in experiments.

In the context of CO_2 sequestration, the chemical composition of the fluids in the reservoir and the degree of reservoir over- or under-pressurization will clearly play a role in the evolution of the permeability of caprock fractures. We contend that leakage, or the development of dissolution-induced preferential pathways is unlikely in the absence of fractures due to the extremely low intact permeability of most caprock formations. Smith et al. [2013] subjected intact cores from the same formation to flow of a CO_2-equilibrated brine and observed the formation of wormholes due to preferential dissolution of dolomite within the core. However, their experiments required excessively large pressure gradients (700 Bar/m), and most likely unsustainable in the field, to induce flow through the low-permeability ($\sim 10^{-19}\mathrm{m}^2$) cores.

5. Concluding Remarks

Our results highlight the influence of the transport and reactive times scales, τ_a and τ_r respectively, even during experiments where significant reactions within the rock matrix were expected ($\tau_d/\tau_r \ll 1$). For smaller values of τ_a/τ_r, our experiments point at fractured dolomitic anhydrite self healing due to a combination of anhydrite dissolution and compaction of the core caused by normal stresses. However, when using lab-scale experiments to infer expected field-scale behavior, it is critical to consider the scaling behavior of different mechanisms. We note that τ_a/τ_r increases with the fracture length, L, which suggests the potential for channel formation and increasing likelihood of persistent leakage pathways at the field-scale. Furthermore, the constant-flow boundary conditions used in our experiments, and many other experimental studies, led to relatively constant τ_a/τ_r over the duration of the experiment. In the field, constant pressure boundary conditions may be more appropriate. Under such conditions, decreasing permeability caused by healing mechanisms will lead to reduced flow and increased τ_a/τ_r, in turn increasing

the potential for the formation of preferential channels. The concurrent compaction of dolomite surrounding the fracture introduces an additional time scale, which further influences the permeability evolution of fractures. These scaling behaviors argue against the likelihood of fractured caprocks healing by the combined influence of chemical reactions and mechanical deformation because an increased τ_a/τ_r is favorable under reservoir conditions.

In addition to implications for permeability evolution relevant to greenhouse-gas sequestration [Wilson and Monea, 2004; Metz et al., 2005; Haszeldine, 2009], our results showing significant alteration of the porous matrix adjacent to fractures highlight a significant alteration of the rock strength [Wintsch et al., 1995]. For the hydrostatic stress applied in our experiments, the dissolution process resulted in significant normal deformation of the fractures. Such significant dissolution-induced deformation in the subsurface can redistribute stresses, which may further alter fracture permeability.

Acknowledgments We gratefully acknowledge financial support from the U.S. Department of Energy, Office of Energy Sciences, Geosciences Program (DE-FG02-09ER16003), the Petroleum Technology Research Center, the IEA GHG Weyburn-Midale CO_2 Monitoring and Storage Project. We also acknowledge the UC Irvine Metrohm Lab for ion chromatography measurements and the Imaging Physics Laboratory at UC Irvine for the x-ray CT-scan. We thank B. Sanders, T. Jones, S. Breen, and E. Brodsky for comments on early versions of this manuscript.

References

Ameli, P., Elkhoury, J. E., Detwiler, R. L., 2013. High resolution fracture aperture mapping using optical profilometry. Water Resour. Res. 49, 1–7.

Bachu, S., 2000. Sequestration of CO_2 in geological media: criteria and approach for site selection in response to climate change. Energy Conversion and Management 41 (9), 953 – 970.

Bandis, S. C., Lumsden, A. C., Barton, N. R., 1983. Fundamentals of rock joint deformation. Int. J. Rock Mech. Mining Sci. 20 (6), 249–268.

Bear, J., 1972. Dynamics of Fluids in Porous Media. Dover.

Berkowitz, B., 2002. Characterizing flow and transport in fractured geological media: A review. Adv. Water Resour. 25 (8-12), 861–884.

Brown, S. R., 1987. Fluid flow through rock joints: the effect of surface roughness. Journal of Geophysical Research 92 (B2), 1337–1347.

Burrowes, G., Gilboy, C., 2001. Investigating sequestration potential of carbonate rocks during tertiary recovery from a billion barrel oil field, Weyburn, Saskatchewan: the geoscience framework. Tech. rep., IEA Weyburn CO_2 Monitoring and Storage Project.

Candela, T., Renard, F., Bouchon, M., Schmittbuhl, J., Brodsky, E. E., 2011. Stress drop during earthquakes: Effect of fault roughness scaling. Bull. Seismo. Soc. Am. 101 (5), 2369–2387.

Chaudhuri, A., Rajaram, H., Viswanathan, H., 2008. Alteration of fractures by precipitation and dissolution in gradient reaction environments: Computational results and stochastic analysis. Water Resour. Res. 44 (10), W10410.

Cook, N. G. W., 1992. Natural joints in rock: Mechanical, hydraulic and seismic behaviour and properties under normal stress. Int. J. Rock Mech. Mining Sci. 29 (3), 198–223.

Detwiler, R. L., 2008. Experimental observations of deformation caused by mineral dissolution in variable-aperture fractures. J. Geophys. Res. 113 (B8), B08202.

Detwiler, R. L., Glass, R. J., Bourcier, W. B., 2003. Experimental observations of fracture dissolution: The role of peclet number on evolving aperture variability. Geophys. Res. Lett. 30 (12), 1648.

Durham, W. B., Bonner, B. P., 1994. Self-propping and fluid flow in slightly offset joints at high effective pressures. J. Geophys. Res. 99 (B5), 9391–9399.

Durham, W. B., Bourcier, W. L., Burton, E. A., 2001. Direct observation of reactive flow in a single fracture. Water Resour. Res. 37, 1–12.

Elkhoury, J. E., Ameli, P., Detwiler, R. L., 2013. Dissolution and deformation in fractured carbonates caused by flow of CO_2-rich brine under reservoir conditions. Int. J. Greenhouse Gas Control 16S, S203–S215.

Elkhoury, J. E., Brodsky, E. E., Agnew, D. C., 2006. Seismic waves increase permeability. Nature 441, 1135–1138.

Elkhoury, J. E., Niemeijer, A., Brodsky, E. E., Marone, C., 2011. Laboratory observations of permeability enhancement by fluid pressure oscillation of in situ fractured rock. J. Geophys. Res. 116, B02311.

Ellis, B. R., Fitts, J. P., Bromhal, G. S., McIntyre, D. L., Tappero, R., Peters, C. A., 2013. Dissolution-driven permeability reduction of a fractured carbonate caprock. Env. Eng. Sci. 30 (4), 187–193.

Faoro, I., Niemeijer, A., Marone, C., Elsworth, D., 2009. Influence of shear and deviatoric stress on the evolution of permeability in fractured rock. J. Geophys. Res. 114, B01201.

Hangx, S. J. T., Spiers, C. J., Peach, C. J., 2010. The effect of deformation on permeability development in anhydrite and implications for caprock integrity during geological storage of CO_2. Geofluids 10, 369–387.

Haszeldine, R. S., 2009. Carbon capture and storage: How green can black be? Science 325 (5948), 1647–1652.

Hitchon, B., Gunter, W. D., Gentzis, T., Bailey, R. T., 1999. Sedimentary basins and greenhouse gases: a serendipitous association. Energy Conversion and Management 40 (8), 825 – 843.

Kumar, A., Ozah, R., Noh, M., Pope, G. A., Bryant, S. Sepehrnoori, K., 2005. Reservoir simulation of CO_2 storage in deep saline aquifers. Soc. Petrol. Eng. J. 10 (3), 336–348.

Liu, E., 2005. Effects of fracture aperture and roughness on hydraulic and mechanical properties of rocks: implication of seismic characterization of fractured reservoirs. J. Geophys. Eng. 2 (1), 38–47.

Lowell, R. P., Van Cappellen, P., Germanovich, L. N., 1993. Silica precipitation in fractures and the evolution of permeability in hydrothermal upflow zones. Science 260 (5105), 192–194.

Mallikamas, W., Rajaram, H., 2005. On the anisotropy of the aperture correlation and effective transmissivity in fractures generated by sliding between identical self-affine surfaces. Geophys. Res. Lett. 32 (11), L11401.

Mason, H. E., Du Frane, W. L., Walsh, S. D. C., Dai, Z. R., Charnvanichborikarn, S., Carroll, S. A., 2013. Chemical and mechanical properties of wellbore cement altered by CO_2-rich brine using a multianalytical approach. Environ. Sci. Tech. 47 (3), 1745–1752.

Metz, B., Davidson, O., de Coninck, H., Loos, M., Meyer, L. (Eds.), 2005. IPCC. Special Report on Carbon Dioxide Capture and Storage. Cambridge University Press.

Noiriel, C., Gouze, P., Madé, B., 2013. 3D analysis of geometry and flow changes in a limestone fracture during dissolution. J. Hydrology 486, 211–223.

Parkhurst, D. L., Appelo, C. A. J., 1999. User's guide to PHREEQC (version 2) - a computer program for speciation, reaction-path, 1D-transport, and inverse geochemical calculations. Tech. Rep. Inv. Rep. 99-4259, US Geol. Surv. Water Resour.

Pluymakers, A. M. H., Peach, C. J., Spiers, C. J., 2014. Diagenetic compaction experiments on simulated anhydrite fault gouge under static conditions. J. Geophys. Res. 119 (5), 4123–4148.

Polak, A., Elsworth, D., Liu, J., Grader, A. S., 2004. Spontaneous switching of permeability changes in a limestone fracture with net dissolution. Water Resour. Res. 40, W03502.

Renard, F., Mair, K., Gundersen, O., 2012. Surface roughness evolution on experimentally simulated faults. J. Struct. Geol. 45, 99–110.

Smith, M. M., Sholokhova, Y., Hao, Y., Carroll, S. A., 2013. Evaporite caprock integrity: An experimental study of reactive mineralogy and pore-scale heterogeneity during brine-CO2 exposure. Environ. Sci. Tech. 47 (1), 262–268.

Szymczak, P., Ladd, A. J. C., 2011. The initial stages of cave formation: Beyond the one-dimensional paradigm. Earth Planet. Sci. Lett. 301 (3-4), 424–432.

Szymczak, P., Ladd, A. J. C., 2012. Reactive-infiltration instabilities in rocks. fracture dissolution. J. Fluid Mech. 702, 239–264.

Tsang, C.-F., Birkholzer, J., Rutqvist, T., 2008. A comparative review of hydrologic issues involved in geologic storage of CO_2 and injection disposal of liquid waste. Environ. Geology 54, 1723–1737.

Wang, J. S. Y., Narasimhan, T. N., Scholz, C. H., 1988. Aperture correlation of a fractal fracture. J. Geophys. Res. 93 (B3), 2216–2224.

Wigand, M., Kazsuba, J. P., Carey, J. W., Hollis, W. K., 2009. Geochemical effects of CO_2 sequestration on fractured wellbore cement at the cement/caprock interface. Chem. Geol. 265, 122–133.

Wilson, M., Monea, M. (Eds.), 2004. IEA GHG Weyburn CO_2 Monitoring & storage project: Summary report 2000-2004. Regina, Saskatchewan, Canada.

Wintsch, R. P., Christoffersen, R., Kronenberg, A. K., 1995. Fluid-rock reaction weakening of fault zones. J. Geophys. Res. 100 (B7), 13021–13032.

Yasuhara, H., Elsworth, D., Polak, A., 2004. Evolution of permeability in a natural fracture: Significant role of pressure solution. J. Geophys. Res. 109, B03204.

Appendix A. Chemical Analysis

Dissolution of a mixture of anhydrite and dolomite involves the following primary reactions:

$$\mathrm{MgCa(CO_3)_2 + H^+ \longleftrightarrow MgCO_3 + Ca^{2+} + HCO_3^-} \tag{A.1}$$

$$\mathrm{MgCO_3 + H^+ \longleftrightarrow Mg^{2+} + HCO_3^-} \tag{A.2}$$

$$\mathrm{CaSO_4 \longleftrightarrow Ca^{2+} + SO_4^{2-}} \tag{A.3}$$

This suggests that when only anhydrite is dissolving, concentrations of Ca^{2+} and SO_4^{2-} should be equal as observed in our experiments (Figure 9).

Results from speciation calculations using PHREEQC [Parkhurst and Appelo, 1999] at conditions representative of our experiments and the Weyburn reservoir (Figure **??**) show the range of potential equilibrium concentrations for different ions. At small pCO_2 dolomite dissolution is negligible (Figure S6a). However, under reservoir conditions, still the amount of dissolved anhydrite is larger than that of dolomite since $SO_4^{2-} > Mg^{2+}$ (Figure S6b). The equilibrium concentrations are relatively insensitive to the presence of other ions but responsive to the increased pressure [Parkhurst and Appelo, 1999]. Note that high values of pCO_2 under the experimental conditions are meaningless since it would be impossible to have $\log(pCO_2) > 0$ under these conditions. The corresponding pH curves are shown in Figure S7. The speciation results highlight the relevance of our experimental results to reservoir conditions as they show a clear range of realistic conditions under which dolomite dissolution will be limited (Figure S6). Note, Hangx et al. [2010] describe preliminary batch experiments in which they quantified $CaCO_3$ precipitation in anhydrite samples at elevated pCO_2; all of the calculations presented here yielded a positive saturation index for $CaCO_3$ which supports the potential for $CaCO_3$ precipitation. However, our calculations suggest the saturation index decreases with increasing pCO_2 due to increased carbonic acid in solution.

Appendix B. Estimating Permeability of EV2 using Kozeny-Carman

We use the Kozeny-Carman equation to estimate the permeability range of sample EV2 as an exercise that shows order of magnitude consistency between measured and estimated values of permeability. The Kozeny-Carman equation

$$Q = -d_e^2 \left[\frac{n^3}{(1-n)^2} \frac{W\,d}{180\,\mu} \right] \nabla P$$

relates the flow rate Q and pressure gradient ∇P across the sample where d is the diameter of the core, W the thickness of the dolomite layer, μ the viscosity of the fluid, n the porosity and d_e the grain size [Bear, 1972]. Using values of $Q = Q_{EV2} = 0.6\,\mathrm{ml/min}$, $W \sim 800\,\mu\mathrm{m}$ and $n = 0.3$, $\mu = 10^{-3}$ Pa s, and sample length $L = 4.9$ cm. The range of grain sizes, d_e, was estimated qualitatively by optical means to be 3 - 12 μm. The grain sizes range yields pressure differences ΔP range of 365 - 5835 kPa. The measured pressure difference of 700 kPa is well within the estimated range (Figure 2). The high porosity is qualitatively consistent with the ease with which most of the dolomite could be brushed off the sample after separating and drying the two halves.

In order to express our results as a permeability range, we use Darcy's law to relate the estimated pressure gradient range to permeability values. For EV2, the estimated pressure range and the imposed flow rate, Q_{EV2}, produce the reported range of permeability in the text; 7.5x10^{-17} - 1.2x10^{-15} m^2 which encompasses the measured value of 6.1x10^{-16} m^2 (Figure 2).

Appendix C. Supplementary material

Supplementary material related to this article can be found on- line at `http://dx.doi.org/10.1016/j.epsl.2015.02.010`.

Can a Fractured Caprock Selfheal?

Supplementary material

Jean E. Elkhoury[1], Russell L. Detwiler[2], Pasha Ameli

Department of Civil & Environmental Eng., University of California, Irvine, CA, USA.

This document of supplementary material includes a set of additional figures that complements those presented in the main text. Each figure is referenced properly in the main text and has a detailed figure caption.

[1]Current address: Schlumberger-Doll Research, Cambridge, MA, USA.

[2]Corresponding author: detwiler@uci.edu

	EV1	EV2
Flow Rate, Q [ml/min]	0.01	0.6
Duration [days]	180	7
Permeability, κ [m^2]		
Before	$\sim$ 2.0x10^{-15}	5.6x10^{-14}
After	$\sim$ 2.0x10^{-15}	6.1x10^{-16}
Initial Diameter [cm]	3.8	3.8
Length [cm]	6.3	4.9
Initial Mass [g]	213	163

Table S1: Summary of the experimental parameters.

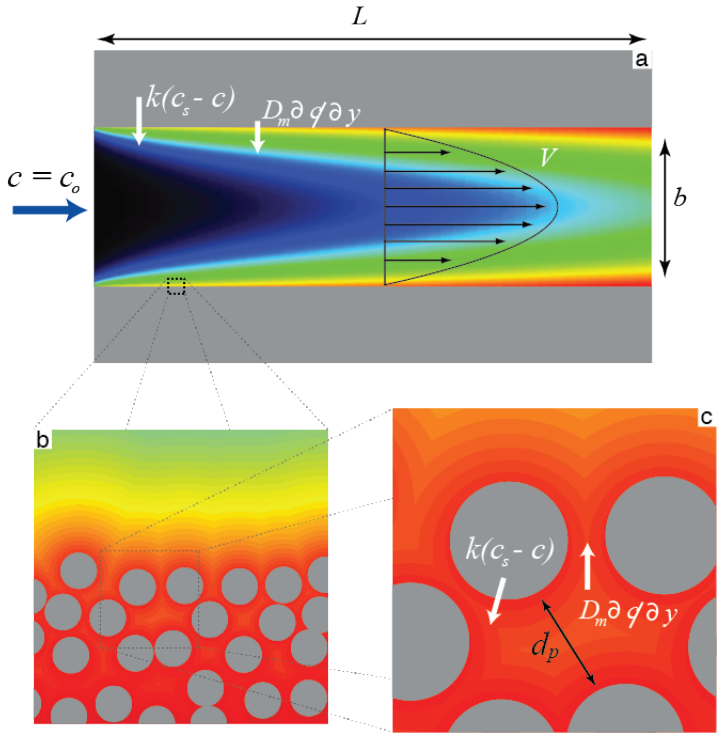

Figure S1: Schematic diagram of a simple fracture with mean aperture b and length L showing the main processes involved in the dissolution of the fracture surfaces and adjacent porous matrix. a) ions dissociate from the fracture surface due to thermodynamic disequilibrium at the mineral surface (k), ions diffuse away from the surface due to the concentration gradient created by the dissolution reaction (D_m) and ions are transported through the fracture by advection (V). The corresponding Damköhler number is given in terms of the advective and reactive time scales $Da^F = \tau_a/\tau_r^F$ where $\tau_a = L/V$ and $\tau_r^F = b/k$. When reaction kinetics are relatively slow, significant reactions may occur within the porous matrix (panels b and c). In this case, ions dissociate from the matrix grains (k) and diffuse away (D_m) through the matrix pores (d_p). Therefore, an additional Damköhler number $Da^M = \tau_d/\tau_r^M$, where $\tau_d = d_p^2/D_m$ and $\tau_r^M = d_p/k$, can be introduced. Color scale represents ions concentration. Black corresponds to concentration $c = c_o$ and red to $c = c_s$.

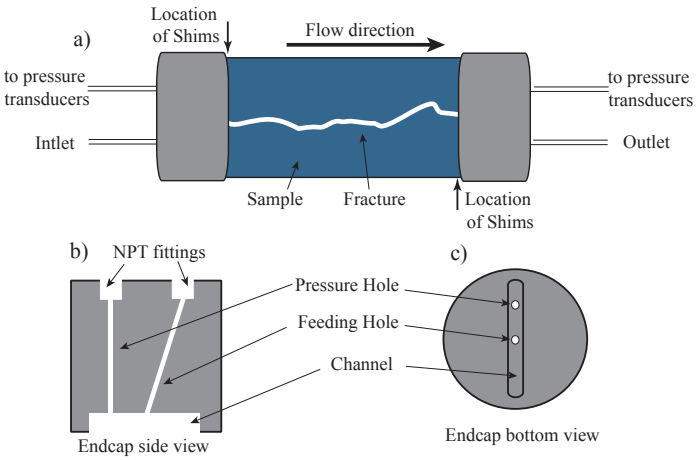

Figure S2: Schematic diagram of the sample assembly. a) Sample is wrapped with a Viton layer and jacketed with a heat shrinking teflon tube before placing in the vessel. The channel in the endcaps is aligned with the fracture (panels b and c). The channel is 0.7 cm deep and wide and 3.2 cm long and fed by a hole in the middle of the channel (panels b and c). The additional hole in the channel is directly connected to pressure transducers (panels b and c).

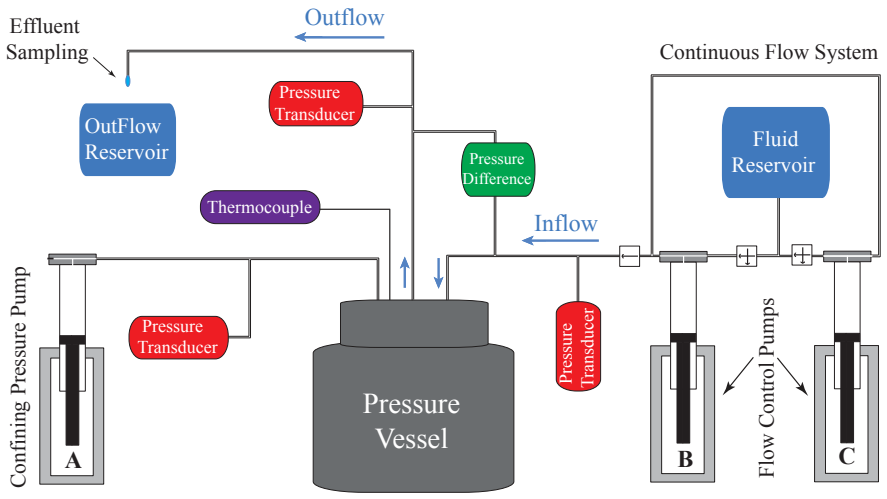

Figure S3: Schematic diagram of the experimental setting. A jacketed fractured anhydrite sample (Figure **??**a) is placed in the pressure vessel. Pump **A** provides the confining fluid and controls the confining pressure applied to the sample. Pumps **B** and **C** provide continuous flow through the sample. The blue arrows denote flow direction. Pressure transducers measure inlet, outlet, differential and confining pressures. A thermocouple placed next to the sample inside the pressure vessel monitors the temperature of the sample. We measured ion concentration in effluent samples collected at the outflow. Pumps, transducers and the thermocouple are controlled and monitored by a computer via Labview.

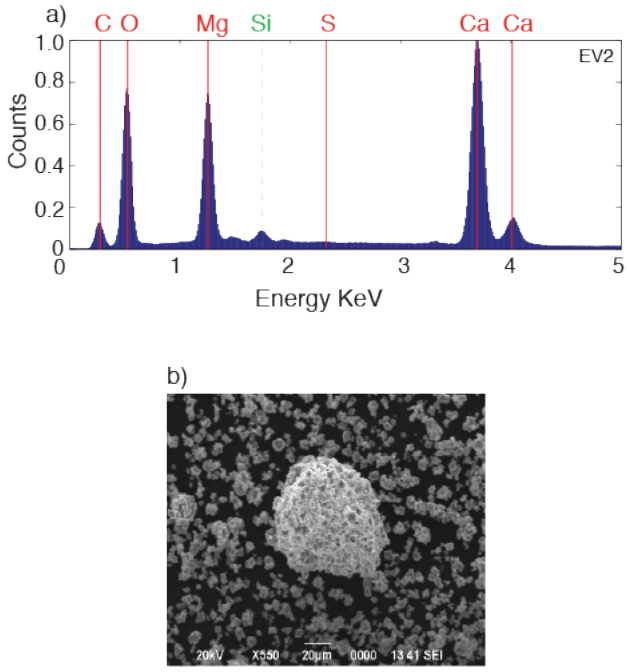

Figure S4: (a) EDS spectrum and (b) SEM image of the powder brushed off sample EV2 after the flow-through experiment and pulling apart the two halves of EV2. It is plain the lack of anhydrite given the absence of the sulfur, S, peak.

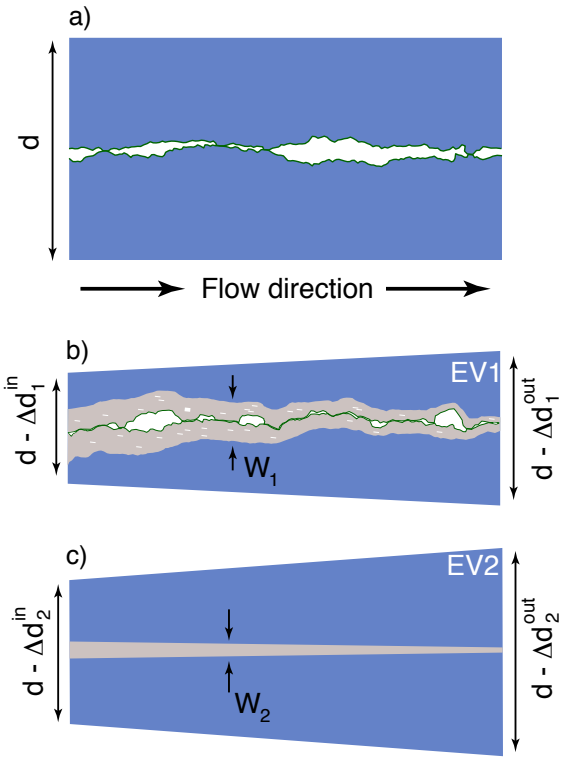

Figure S5: Schematic diagram (not to scale) of the change in sample geometry due to the reactive flow through the fractured samples. Color key is as follow: anhydrite is blue, fracture profiles are green, aperture regions are white and dolomite is gray. b) Sample EV1 was subject to low flow rate which reduced the aperture field at some locations and enhanced it at others evident by the localized dissolution and the lack of the strong permeability reduction (Figures 5 - 8). Dispersed white segments represent voids observed in the optical photographs (Figure 7) and SEM images (Figure 8b). These could be connected and thus might provide additional flow paths. c) On the other hand, sample EV2 was subject to high flow rate leading to the closure of the aperture field and fracture healing (Figures 2 and 3). Diameter perpendicular to the fracture, in both samples, was reduced (Figure 4) and represented schematically here; $\Delta\, d_1^{in} = 700$, $\Delta\, d_1^{out} = 450$, $\Delta\, d_2^{in} = 330$ and $\Delta\, d_2^{out} = 20$. Dashed lines in panel b) represent the diffusive edge of the dolomite layer of thickness $W_1 \sim 4000\,\mu$m. The dolomite layer in panel c) is of width $W_2 \sim 800\,\mu$m.

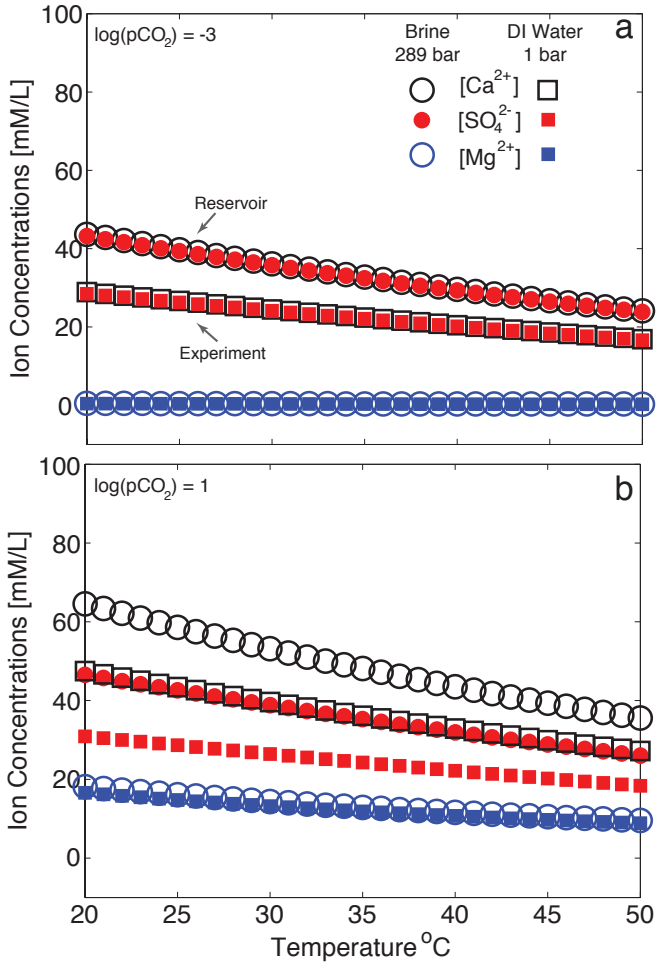

Figure S6: Equilibrium concentrations of Ca^{2+} (black), SO_4^{2-} (red), and Mg^{2+} (blue) under experimental conditions (deionized water at 1 bar pore pressure) (circles) and reservoir conditions (brine at 289 bar pore pressure) (squares). a) shows results for $\log(pCO_2) = -3$ and b) for $\log(pCO_2) = 1$.

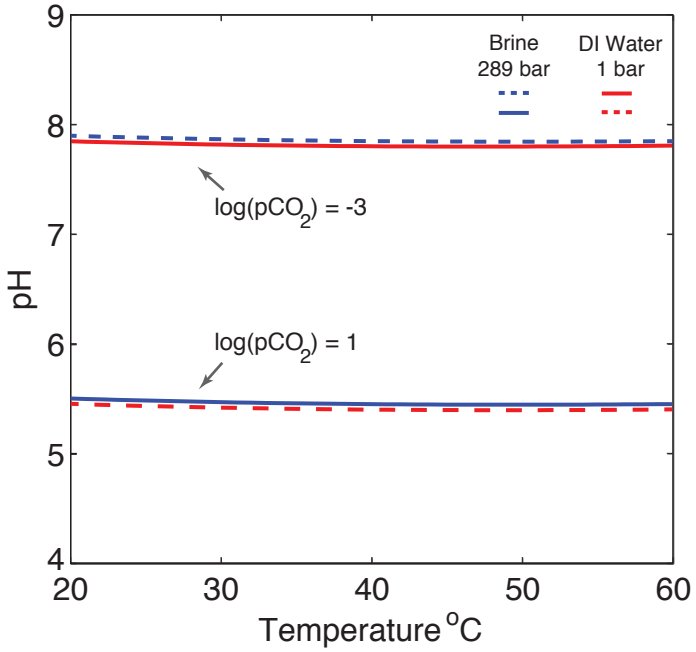

Figure S7: pH under reservoir conditions (brine at 289 bar) (blue) and experimental conditions (deionized water at 1 bar pore pressure) (red) for $\log(\mathrm{pCO_2}) = -3$ and $\log(\mathrm{pCO_2}) = 1$.